International Journal of Mechanical Sciences 180 (2020) 105753

Contents lists available at ScienceDirect

International Journal of Mechanical Sciences

journal homepage: www.elsevier.com/locate/ijmecsci

Modeling SMA-enabled soft deployable structures for kirigami/origami reflectors

Ning An [a], Meie Li [b,*], Jinxiong Zhou [a]

[a] State Key Laboratory for Strength and Vibration of Mechanical Structures and School of Aerospace, Xi'an Jiaotong University, Xi'an 710049, People's Republic of China
[b] State Key Laboratory for Mechanical Behavior of Materials, School of Materials Science and Engineering, Xi'an Jiaotong University, Xi'an 710049, People's Republic of China

ARTICLE INFO

Keywords:
Kirigami/origami reflectors
Soft deployable structures
Smart soft composites
Shape memory alloy
Finite element method

ABSTRACT

The synergic combination of smart soft composites with kirigami/origami principles leads to self-deployable systems. To date, the development of soft deployable structures has largely been an empirical process. Focusing on the recently developed shape memory alloy (SMA)-based soft deployable structures, this paper describes an analytical model and a finite element (FE) numerical scheme to investigate deformation and deployment performance of this system. The study provides insights into the working principles of these soft deployable structures by understanding how the system deforms as a function of the SMA recovery strain for a number of geometrical parameters. The FE method was further used to simulate the fabrication and deployment process of three types of kirigami/origami reflectors. The realization of a two-step scheme, i.e., predeformation of the deployable frame and then the concurrent deformation of both frame and kirigami/origami films, is detailed herein. This makes our simulation capable of capturing the features of SMA-based soft deployable structures observed in experiments, and also renders the prediction versatile and manufacturing-oriented. We expect the work would enhance the understanding of soft deployable structures, and may open the door for design and fabrication of soft robotics and machines.

1. Introduction

Kirigami/origami - the ancient art of paper cutting and folding - has been a surge in research interests from physicists, mathematicians and engineers, as it not only enables the design of functional materials with novel properties, including negative and tunable Poisson's ratio [1], programmable shape [2,3], and mechanical response [4], and multistability [5], but also leads to the development of novel structures with applications in the fields of soft robotics [6,7] and aerospace engineering [8,9]. A key feature of these kirigami/origami-inspired materials and structures is that they are conveniently cut or folded when flat and then deformation-driven pattern transformation can be exploited to create complex 3D configurations. The core challenge in the design of kirigami/origami-inspired structures is where and how to assign cuts and creases to obtain a predefined pattern that deploys/folds into a given 3D shape. Unsurprisingly, many methods have been proposed for performing this task such as the *tuck-folding method* for origami [10–13] and the inverse design method for kirigami [2,14] which allows for design of both convex and non-convex kirigami/origami surfaces.

Kirigami/origami techniques offer an elegant approach to design reconfigurable and deployable reflectors with potential use in aerospace and other industries, for example, Liu et al. proposed a design of an origami reconfigurable quadrifilar helical antenna with a foldable reflector that could operate over the K, Ka, and extremely high-frequency bands [15]. However, this type of structure typically requires an external mechanical force to trigger transformation of configurations and a particular type of traditional external systems that be used to deploy origami reflectors is the inflatable booms [16,17]. Interestingly, it has also been shown that the integration of smart soft composites into kirigami/origami techniques - thus giving rise to self-deployable systems - helps to reduce the mechanical complexity and implementation requirements involved in triggering the pattern transformation. One particular type of smart soft composite structures is derived from the combination of smart materials with soft elastomeric materials. This synergic combination results in systems that are soft, self-deployable, and programmable. Current strategies include the use of stimuli responsive hydrogels [18,19], liquid crystal elastomers [20–22], and shape memory materials [23–26]. Among them, fabrication and actuation of SMA-based smart soft composites is simpler and more controllable and have the advantage of high power density [27,28]. A variety of soft actuators that capable of complex deformation (i.e., bending, twisting, or a bend/twist coupled motion) have been demonstrated by embedding SMA wires into a soft matrix [29–32]. Very recently, Wang et al. successfully fabricated self-deployable mirrors that reflect sunlight by integrating SMA-enabled soft deployable structures as a frame with kirigami/origami-inspired foldable reflective films [33–35]. Note

* Corresponding author.
E-mail address: limeie@mail.xjtu.edu.cn (M. Li).

https://doi.org/10.1016/j.ijmecsci.2020.105753
Received 6 February 2020; Received in revised form 3 May 2020; Accepted 4 May 2020
Available online 7 May 2020

that compared with existing geometrically complex self-folding active origami reflector designs with bellows [12,13,36,37], the integrating self-deployable reflector systems proposed by Wang et al. [34] and studied in this manuscript could be more controllable as it avoids actuating a number of origami hinges but need only one applied current to deform the SMA-based frame.

While empirical approaches have highlighted the exciting potentials of SMA-based deployable structures [33–35,38,39], the lack of robust models for the system renders design of SMA-based deployable structures a time-consuming process and can only be realized in a trial-and-error way. Due to the nonlinear response of SMAs, predicting the performance of soft deployable structures integrated with kirigami/origami materials is nontrivial by just using an analytical approach; numerical simulation is supplementary to the analytical approach to model and design the SMA-based self-deployable systems prior to manufacturing. Over the past decades, a substantial number of 3D constitutive models and finite element modeling techniques have been developed to simulate the thermomechanical behavior of SMAs (see the review paper of Cisse et al. [40]). Among them, the Boyd-Lagoudas model [41,42] has been widely used in engineering problems, for the simple assumptions and compatibility with finite element computation. By coding the free energy function and its derivatives into commercially available finite element software in the form of user defined subroutine, the Boyd-Lagoudas model has been widely recognized by the research community and was successfully applied to performance analysis of various SMA-based smart devices, i.e., origami-inspired active structures [37,43], aerospace structues [44] and soft morphing actuators [45–47].

In this study, we propose both analytical and numerical models that predict the performance of SMA-enabled soft deployable structures. In our simulations, the previously developed user subroutine of SMA based on Boyd-Lagoudas model [48] was adopted to correlate the deformation and the phase transition of SMA and the recovery strains were extracted from the simulation. We first study the response of individual bending segments and soft deployable units under various SMA recovery strains. The effects of geometric parameters on the bending or deploying process are explored in details. We then show that by using the soft deployable structure as a frame to stretch kirigami/origami films, we can numerically reproduce the experimentally observed deployment process of kirigami/origami reflectors reported in [34]. To closely follow the experimental fabrication procedure, we also detail here the implementation of numerical simulation by utilizing a function, "model change", provided in the software to model the predeformation of frame and then the concurrent deformation of both frame and films.

The main contribution of this manuscript is to provide an extensive numerical study of the self-deployable reflector systems proposed by Wang et al. [34] and reveal the effect of geometric design parameters on performance of these structures. Our numerical strategy will also aid the design and optimization of these self-deployable kirigami/origami systems and provide crucial insights into the working principles of these systems.

2. Soft deployable structure

The soft deployable structure studied in this work, which was proposed in [34], consists of a series of unit cells, as schematized in Fig. 1(a). Each unit cell is composed of multiple repeating base elements which are arranged in an alternative way and connected together using soft joints [see Fig. 1(b)]. The design of a typical base element, which we refer to as a "bending segment", is made of smart soft composites consisting of a thin SMA wire that is embedded inside a Polydimethylsiloxane (PDMS) matrix with a 3D printed reinforcement made of Acrylonitrile butadiene styrene (ABS) [see Fig. 1(c). More details about the fabrication process can be found in [34]]. The SMA wire is used as an active layer to provide the actuating force to the structure. The ABS reinforcement, serving as a strain-limiting layer, allows the use of a thinner matrix while obtaining larger deformation and a faster recovery speed. The PDMS matrix is used to firmly combine the SMA wire and ABS reinforcement, and control the stiffness of the overall structure. The soft joints are also made from PDMS polymer and are used to connect adjacent deployable unit cells. Note that the SMA wire is prestretched when embedded into the PDMS, and the stretching results in a pseudoelastic deformation of the SMA wire, caused by a detwinning of the martensite phase. Then the SMA wire is going to recover its original shape when the temperature is increased over its austenite phase transition temperature. Therefore, as the SMA wire is heated, it contracts in length while the ABS reinforcement restrains any contraction. To accommodate this mismatch between the SMA wire and ABS reinforcement, the segments bend, and then the unit cell opens due to the alternating eccentricity of the bending segments, and therefore, the full structure exhibits a pattern switch from its original flat shape to a diamond-like configuration. To get deeper insight into the deployment process of the system and be able to efficiently design application-specific soft deployable structures,

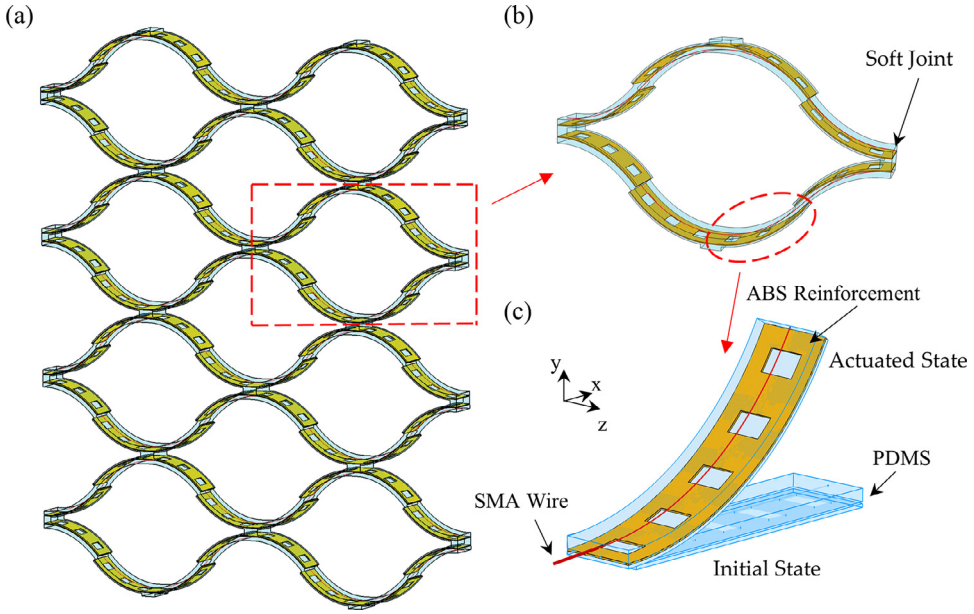

Fig. 1. Schematic of the soft deployable structure. (a) A finite-size deployable structure consists of a series of unit cells. (b) The unit cell consists of multiple repeating base elements (which we refer to as 'bending segments') connected in an alternative way. (c) A bending segment is fabricated by embedding a SMA wire (colored in red) and an ABS reinforcement (colored in beige) in PDMS matrix (colored in light blue). As the SMA wire is heated, it contracts in length while the ABS reinforcement restrains any contraction, causing the bending of the segment. (For interpretation of the references to colour in this figure legend, the reader is referred to the web version of this article.)

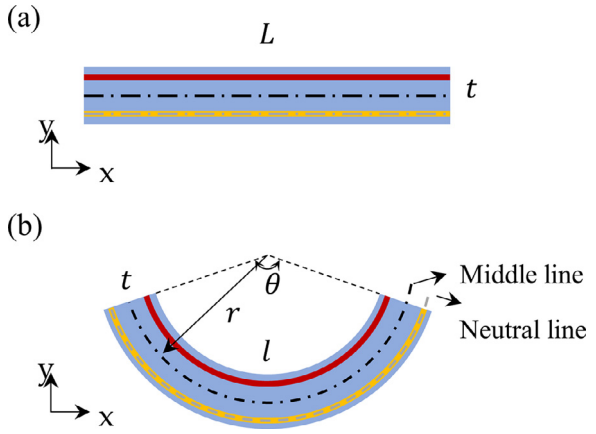

Fig. 2. Geometry of a single bending segment in (a) the initial state and (b) the actuated state.

an analytical model as well as a finite element method (FEM) model are developed in this contribution.

3. Theory and methodology

3.1. Analytical modeling

1) Model for Single Bending Segment: To begin with, we present a simple analytical model to describe the explicit relationship between the recovery strain of SMA wire and the bending curvature of a single segment.

As we can see in Fig. 2(a), upon heated, the SMA wire contracts, shortening the length of the actuating layer:

$$l = L(1-\varepsilon) \tag{1}$$

where L is the initial length in lateral direction of both the actuating layer and the strain-limiting layer, l is the length in lateral direction of the actuating layer upon heated, and ε is the recovery strain of the SMA wire.

While the elastic modulus of ABS is much larger than that of PDMS, then the length of strain-limiting layer can be considered to be unchanged during the bending deformation. Therefore, from Fig. 2 the following geometrical relations are derived when the segment bends from initial [see Fig. 2(a)] to actuated state [see Fig. 2(b)]:

$$l = \theta(r - \frac{t}{2}) \tag{2}$$

$$L = \theta(r + \frac{t}{2}) \tag{3}$$

where θ is the bending angle, r is the radius of curvature of the middle layer, which is located in the middle of the actuating and strain-limiting layer, and t represents the distance between the actuating and strain-limiting layer.

The combination of Eqs. 1, 2 and 3 yields an explicit analytical expression for the bending curvature $\kappa = 1/r$ of the middle layer, i.e.:

$$\kappa = \frac{\varepsilon}{2-\varepsilon} \cdot \frac{2}{t} \tag{4}$$

Eq. 4 indicates that the bending curvature κ is independent of the initial length of the segment L, and for a specific structure with thickness t, the bending curvature κ is entirely determined by the recovery strain of the SMA wire ε.

2) Model for a Deployable Unit Cell: We then derive an expression for the finite macroscopic strains $\bar{\varepsilon}_{xx}$ and $\bar{\varepsilon}_{yy}$ of a deployed unit cell by extending the analytical model previously developed for the single bending segment. As shown in Fig. 3, the macroscopic strains of a deployed unit cell are defined by:

$$\bar{\varepsilon}_{xx} = \frac{L'_x - L_x}{L_x} \tag{5}$$

and

$$\bar{\varepsilon}_{yy} = \frac{L'_y - L_y}{L_y} \tag{6}$$

where $L_x = 2L$ and $L_y = 4t + 2h$ are the initial length of the unit cell in x and y directions, respectively. Note that h is the thickness of the soft joints. Moreover, the current length of the deployed unit cell L'_x and L'_y can be calculated as [see Fig. 3(b)]:

$$L'_x = 4(r - \frac{t}{2})sin\frac{\theta}{2} \tag{7}$$

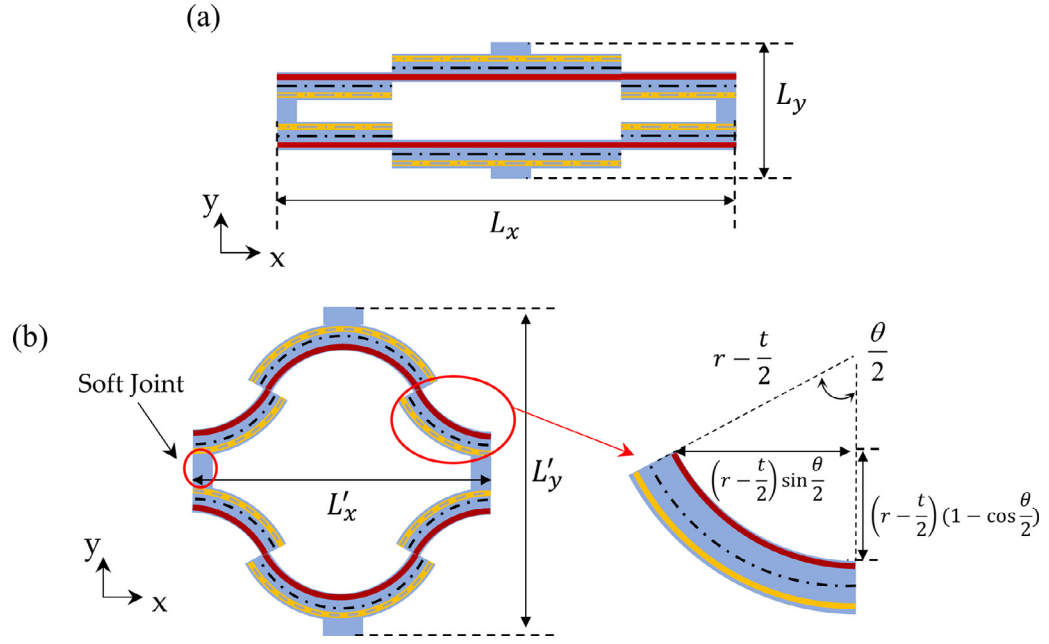

Fig. 3. Geometry of a deployable unit cell in (a) the initial state and (b) the actuated state.

and

$$L'_y = 4(r - \frac{t}{2})(1 - cos\frac{\theta}{2}) + 4t + 2h \tag{8}$$

where θ can be determined by combing Eqs. 3 and 4.

3.2. Finite element method modeling

1) Constitutive model of SMAs: The SMA constitutive model, which was derived by Lagoudas et al. [41,42,48] based on the assumed form of the total Gibbs free energy of a polycrystalline, is used to predict the thermomechanical behavior of SMA in this article.

The total Gibbs free energy is given by:

$$\begin{aligned} G(\boldsymbol{\sigma}, T, \xi, \varepsilon^t) = &-\tfrac{1}{2}\tfrac{1}{\rho}\boldsymbol{\sigma} : \boldsymbol{S} : \boldsymbol{\sigma} - \tfrac{1}{\rho}\boldsymbol{\sigma} : [\alpha(T - T_0) + \varepsilon^t] \\ &+c[(T - T_0) - T\ln(\tfrac{T}{T_0})] - s_0 T + u_0 + f(\xi) \end{aligned} \tag{9}$$

where $\boldsymbol{\sigma}$, ε^t, ξ, T and T_0 are the Cauchy stress tensor, transformation strain tensor, martensitic volume fraction, current temperature and reference temperature, respectively. The material constants $\boldsymbol{S}$, $\boldsymbol{\alpha}$, ρ, c, s_0 and u_0 are the effective compliance tensor, effective thermal expansion tensor, density, effective specific heat, effective entropy at reference state and effective specific internal energy at reference state. The function $f(\xi)$ is the transformation hardening function.

The total strain $\boldsymbol{\varepsilon}$ is given by

$$\boldsymbol{\varepsilon} = \boldsymbol{S} : \boldsymbol{\sigma} + \boldsymbol{\alpha}(T - T_0) + \boldsymbol{\varepsilon}^t \tag{10}$$

The relation between the transformation strain tensor $\boldsymbol{\varepsilon}^t$ and the martensitic volume fraction ξ is expressed by

$$\dot{\boldsymbol{\varepsilon}}^t = \Lambda\dot{\xi} \tag{11}$$

where Λ is the transformation tensor which determines the transformation strain direction.

$$\Lambda = \begin{cases} \frac{3}{2}H\frac{\sigma'}{\bar{\sigma}}, & \dot{\xi} > 0, \\ H\frac{\varepsilon^{t-r}}{\bar{\varepsilon}^{t-r}}, & \dot{\xi} < 0 \end{cases} \tag{12}$$

H is the maximum uniaxial transformation strain, $\boldsymbol{\varepsilon}^{t-r}$ is the transformation strain at the reversal of the transformation.

An additional constraint is obtained in the form of an inequality by the second lat of thermodynamics as

$$\Phi(\boldsymbol{\sigma}, T, \xi) \leq 0 \tag{13}$$

where Φ is a transformation function that is defined in terms of the thermodynamic force π and controls the onset of forward and reverse transformation.

$$\Phi = \begin{cases} \pi - Y^*, & \dot{\xi} > 0, \\ -\pi - Y^* & \dot{\xi} < 0 \end{cases} \tag{14}$$

where Y^* is the measure of internal dissipation due to the phase transformation. When $\Phi < 0$ the material response is elastic and the martensite volume fraction will remain constant ($\dot{\xi} = 0$). During the forward and reverse transformations ($\dot{\xi} \neq 0$) the state of stress, temperature, and martensite volume fraction will remain on the transformation surface, which is characterized by $\Phi = 0$.

Table 1
Material parameters of Flexinol SMA.

Material Parameter	Value
Austenitic Young's modulus E_A	75 GPa
Martensitic Young's modulus E_M	28 GPa
Poisson's ratio (equal for both phases) ν	0.33
Coefficient of thermal expansion for the austenite α^A	22.0E-6 K^{-1}
Coefficient of thermal expansion for the martensite α^M	22.0E-6 K^{-1}
Martensitic start temperature M_s	350 K
Martensitic finish temperature M_f	315 K
Austenite start temperature A_s	354 K
Austenite finish temperature A_f	379 K
Maximum transformation strain H	0.065
Stress influence coefficient for austenite $\rho\Delta s^A$	-0.35 MPa K^{-1}
Stress influence coefficient for martensite $\rho\Delta s^A$	-0.35 MPa K^{-1}

2) FEM Implementation: The constitutive model described above can be implemented into commercial finite element program Abaqus/Standard 2017 through a user defined subroutine UMAT to simulate the thermomechanical response of SMAs for various loading modes. In this study, a previously developed Abaqus SMA_UM subroutine [48] is used. The material parameters required by the SMA_UM subroutine are Young's modulus of both austenite and martensite (E_A and E_M); the martensite start and finish and the austenite start and finish temperatures (M_s, M_f, A_s, and A_f, respectively); the maximum transformation strain (H); and the asutenite and martensite stress influence coefficients ($\rho\Delta s^A$ and $\rho\Delta s^M$, respectively). These parameters were taken from [34] and [48] and summarized in Table 1 and Fig. 4. Moreover, both the ABS reinforcement and the PDMS matrix were modeled as linear elastic materials. In particular, the Young's modulus and Poisson's ratio are $E = 2.6$ GPa and $\nu = 0.35$ for the ABS reinforcement and $E = 1.8$ MPa and $\nu = 0.495$ for the PDMS matrix.

The response of the soft composites was simulated by conducting dynamic implicit simulations (*Dynamic module in Abaqus) and quasi-static conditions were ensured by monitoring the kinetic energy. The temperature loading was applied in an incremental manner and large displacement formulation was used to capture the nonlinear large deformation (NLGEOM = YES in Abaqus) [49]. All the components of the composites were modeled using solid linear reduced-integration hexahedral elements (Abaqus element type C3D8R) with enhanced hourglass control and the accuracy of the mesh was ascertained through a mesh refinement study. The soft deployable structures were modeled in two manners: (1) considering an unit cell of the domain with appropriate periodic boundary conditions and (2) considering the full finite-size deployable structure.

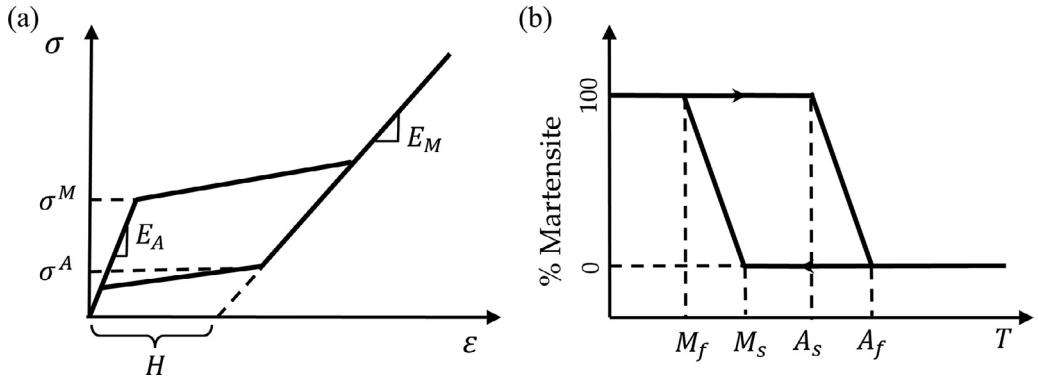

Fig. 4. Definition of the material parameters of Flexinol SMA in (a) an uniaxial pseudoelastic test and (b) thermally-induced phase transformation diagram.

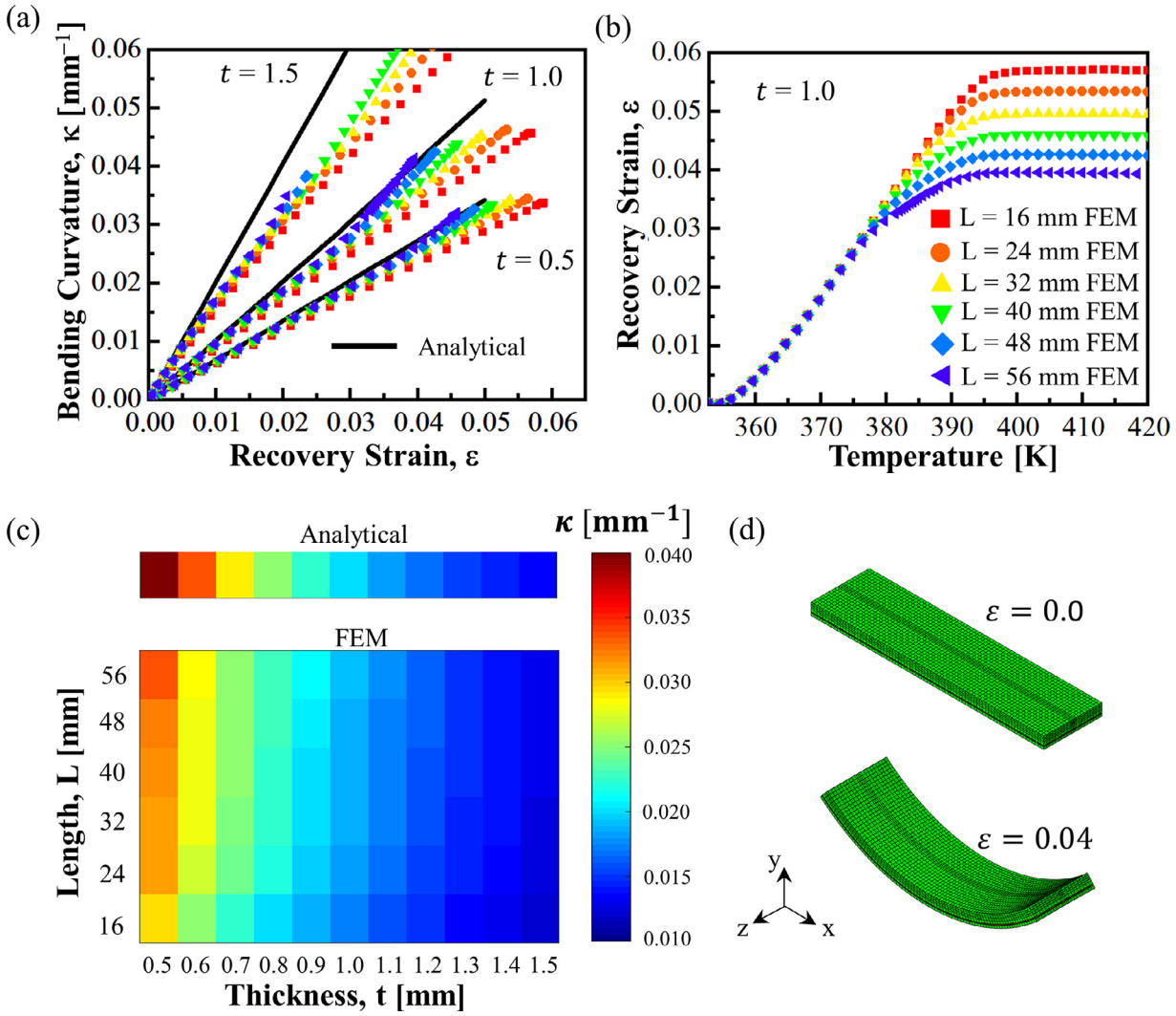

Fig. 5. Bending deformation of individual segments. (a) Evolution of bending curvature κ as a function of the SMA recovery strain ε. Analytical predictions (solid lines) are compared to FEM simulation results (markers). (b) Evolution of SMA recovery strain ε as a function of temperature. (c) Contour plots showing effect of thickness t and length L on the bending curvature κ at $\varepsilon = 0.02$. (d) FEM snapshots showing detailed mesh of a single bending segment characterized by $L = 40$ mm and $t = 1.0$ mm at $\varepsilon = 0$ and 0.04.

4. Results and discussions

4.1. Bending segment

We began by investigating the bending deformation of individual segments characterized by $L \in [16, 56]$ mm and $t \in [0.5, 1.5]$ mm. In these simulations, the individual segments were under free-free boundary conditions, and a temperature load ranging from $T = 353$ K to $T = 420$ K was applied to the SMA wires. As temperature increases, the SMA wire contracts and the individual segment bends. During bending, at every 1 K increment, we acquired coordinates of nodes located at the SMA line and those located at the middle line from the deformed configuration (the definition of the SMA and middle line is shown in Fig. 2). The SMA nodes coordinates were used to calculate the current length and then the recovery strain ε of the SMA wire through Eq. 1; the middle nodes coordinates were used to determine the radius r of the circle that best fits its bent shape [50], and then the bending curvature was given as $\kappa = 1/r$. This deformation and recovery strain correlation technique captures the main physics of SMA phase transition and simplifies the analysis process, and will be used repeatedly in the following simulation of deployable structures and reflectors.

In Fig. 5(a) we report the evolution of bending curvature κ as a function of the SMA recovery strain ε, as predicted by Eq. 4 (solid lines). The analytical results indicate that the curvature increases as recovery strain increases. In Fig. 5(a) the analytical predictions are also compared to FEM results (markers), showing a good agreement and therefore validating our FEM model, and Fig. 5(b) plots the SMA recovery strain versus temperature relation obtained from FEM simulations. We then investigated the effect of geometry (i.e., thickness t and length L) on the bending curvature by fixing recover strain at $\varepsilon = 0.02$. The analytical results, as predicted by Eq. 4 and shown in Fig. 5(c) (top panel), indicate that the bending curvature of the segment is independent on the length and is determined solely by the thickness t of the segment; while the FEM results shown in Fig. 5(c) (bottom panel) indicate that the bending curvature depends highly on thickness t and also depends slightly on length L. This discrepancy between analytical and FEM results is due to boundary effect, which is not accounted for in the analytical model. We report as an example in Fig. 5(d) the initial state and the actuated

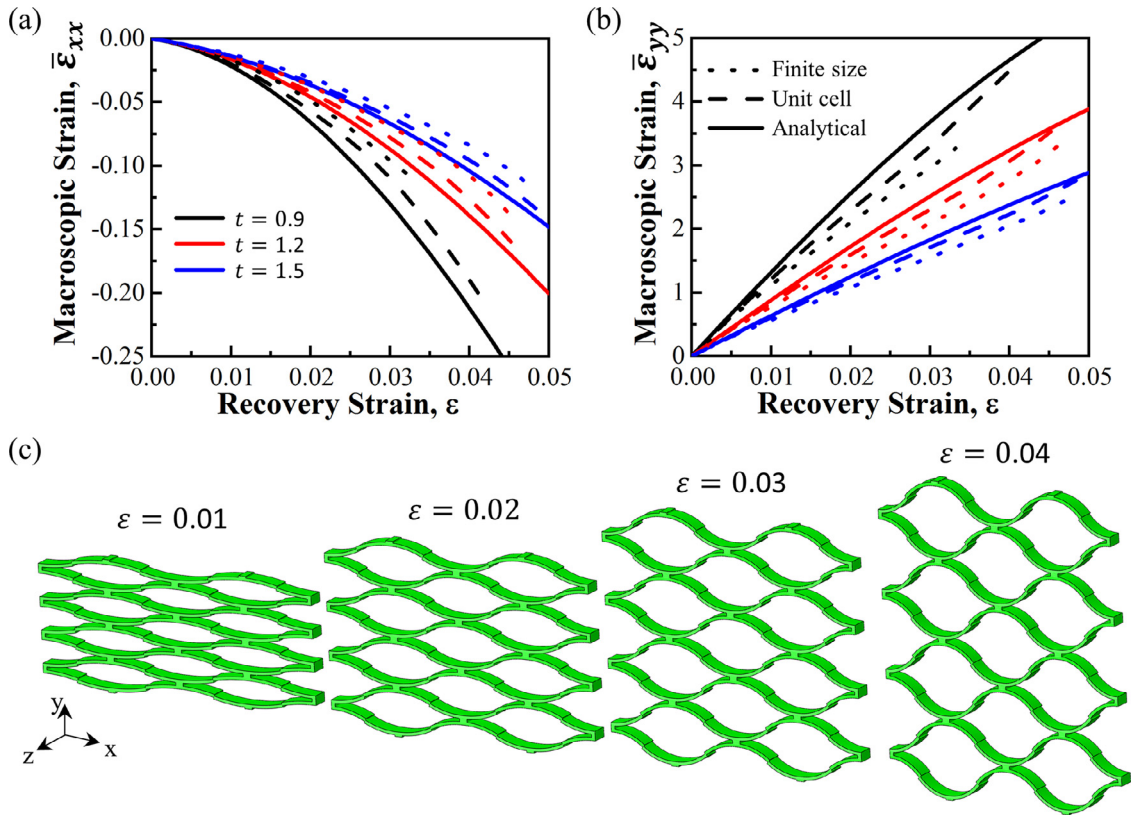

Fig. 6. Deformation of the soft deployable structure. Evolution of macroscopic strain in x (a) and y (b) direction as a function of the SMA recovery strain ε. (c) FEM snapshots of a finite-size deployable structure characterized by $L = 48$ mm and $t = 1.0$ mm at different levels of SMA recovery strain, $\varepsilon = 0.01$, 0.02, 0.03, and 0.04.

state of a single segment with $L = 40$ mm and $t = 1.0$ mm at $\varepsilon = 0.04$, in together with the detailed mesh used in this study.

4.2. Deployable structure

We then move on to explore the deformation of soft deployable structures. A soft deployable structure consists of 8 unit cells and each unit cell is composed of 4 bending segments which are arranged alternatively and connected together using soft joints. As each comprising segment bends under actuation, the unit cell opens with a contraction in x direction and an expansion in y direction. In Figs. 6(a) and 6(b) we report the evolution of macroscopic strains, $\bar{\varepsilon}_{xx}$, $\bar{\varepsilon}_{yy}$, as a function of the SMA recovery strain ε for a number of deployable structures characterized by $L = 48$ mm and $t = 0.9$, 1.2, 1.5 mm. Note that the height of soft joints is fixed as $h = 3.0$ mm throughout this manuscript. The absolute value of $\bar{\varepsilon}_{xx}$ and $\bar{\varepsilon}_{yy}$ increases monotonously as the SMA recovers and $\bar{\varepsilon}_{xx} < 0$ indicates a contraction in x direction. Fig. 6(c) presents the FEM snapshots of a finite-size soft deployable structure at various recover strains $\varepsilon = 0.01$, 0.02, 0.03, and 0.04. The geometry of each segment for this finite-size structure was fixed as $L = 48$ mm and $t = 1.0$ mm.

To reduce the computation cost and ensure the response is not affected by boundary effects, we also consider infinite periodic structures using representative unit cells with suitable periodic boundary conditions. As shown in Figs. 6(a) and 6(b), we find good agreement between the analytical results predicted by the combination of Eqs. 5–8 and the FEM results obtained from both finite-size and unit cell simulations. To better understand the effect of geometry on the deployment process, we then exploit unit cell simulations to fully explore the design space and simulate the response of deployable structures in which each comprising segment is characterized by $L \in [16, 56]$ mm and $t \in [0.5, 1.5]$ mm. In Fig. 7 we report as contour plots the macroscopic strain in x and y directions of deformed soft deployable structures at $\varepsilon = 0.02$. The analytical and FEM results shown in Fig. 7 confirm that by tuning t and L we can alter the deployment of the structure. Specifically, we find that a lower value of t or a larger value of L leads to a larger absolute value of $\bar{\varepsilon}_{xx}$ and $\bar{\varepsilon}_{yy}$.

4.3. Kirigami/origami reflectors

Having demonstrated the structural design and the continuous and controllable deployment process of the soft deployable structures, we now show that the soft deployable structures can be exploited to design kirigami/origami-based self-deployable reflectors. The method is to integrate kirigami/origami reflective films with a soft deployable structure and use the soft deployable structure as a frame to stretch kirigami/origami films [34]. In real fabrication and application, in order to maximize the deployed/stowed size ratio, the deployable system should be fabricated to be as compact as possible when stowed as large as possible when deployed. This imposes difficulties for deployable kirigami reflectors and also explains the difference between kirigami and origami reflectors. For kirigami designs, the kirigami films should maintain a finite area in the undeformed state due to the stretchability limit of the film material. Therefore, in real fabrication and experiment in [34], the SMA deployable frame was deformed a little bit to accommodate the initial size of the kirigami films, prior to the assembly of the frame/film system. This predeformation of the frame and the following concurrent deformation of the frame/film system should be handled properly in simulation. In contrast, for origami designs proposed herein, the predeformation of the SMA actuated frame is unnecessary since the origami film can be compressed compactly with negligible size or volume and inserted and connected to the frame directly.

It is not straightforward to model the above-mentioned sequential deformation of kirigami reflector design where the frame and film are assembled together but undergo different deformations. In addition, both

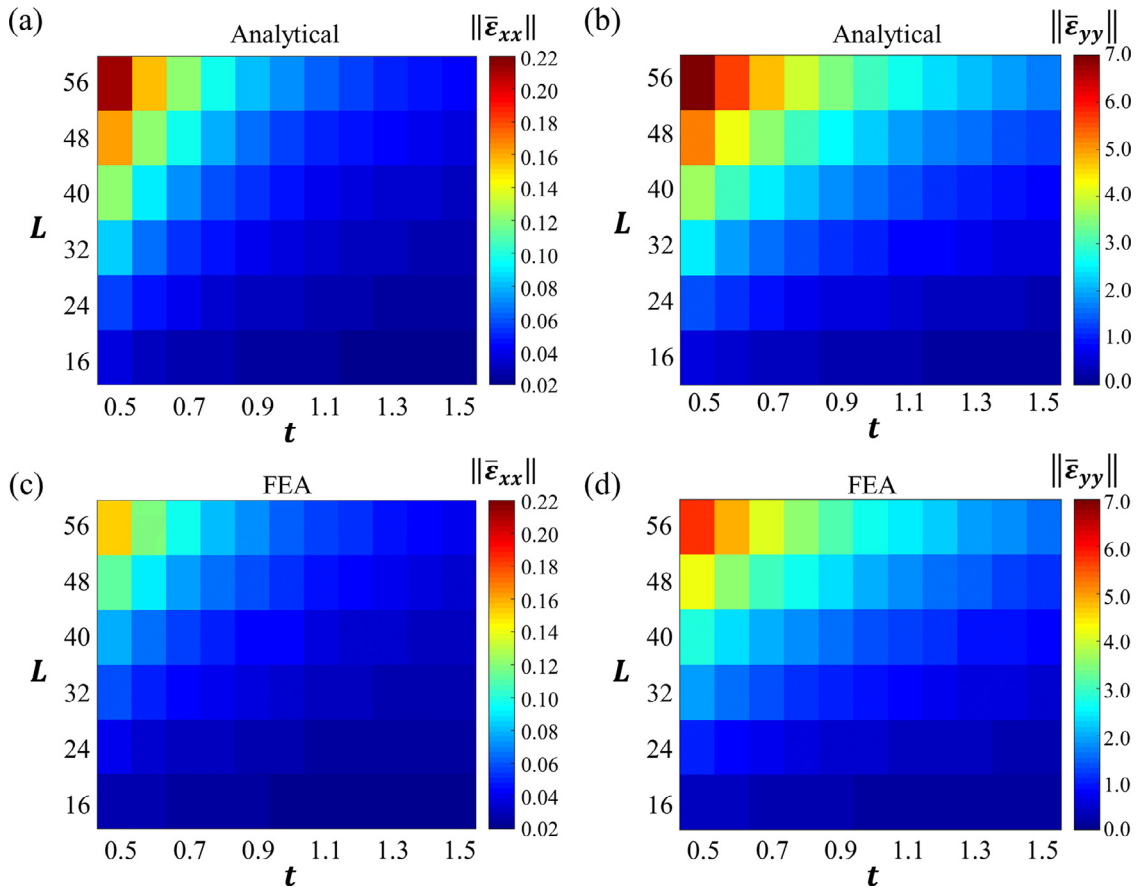

Fig. 7. Effect of geometry (i.e., thickness t and length L of comprising individual segments) on the macroscopic strain in x and y direction, respectively. (a) and (b) Analytical results. (c) and (d) FEM results.

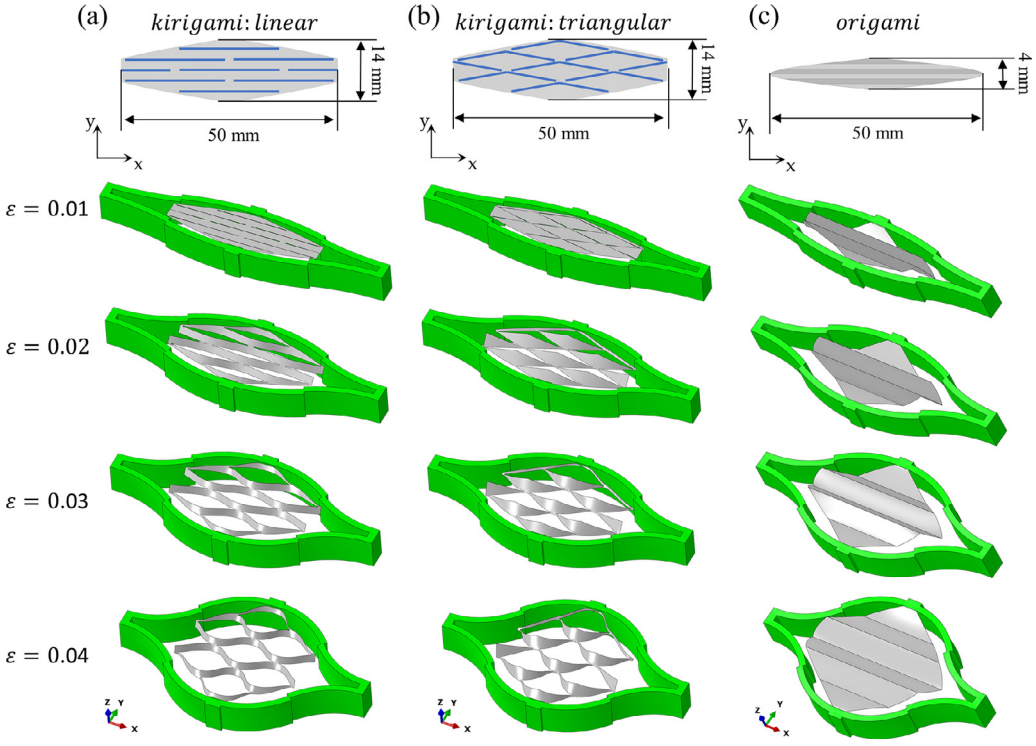

Fig. 8. Design and deformation of self-deployable reflector units under various SMA recovery strains. (a) Deployment of a kirigami reflector unit with linear cut pattern. (b) Deployment of a kirigami reflector unit with triangular cut pattern. (c) Deployment of a origami reflector unit.

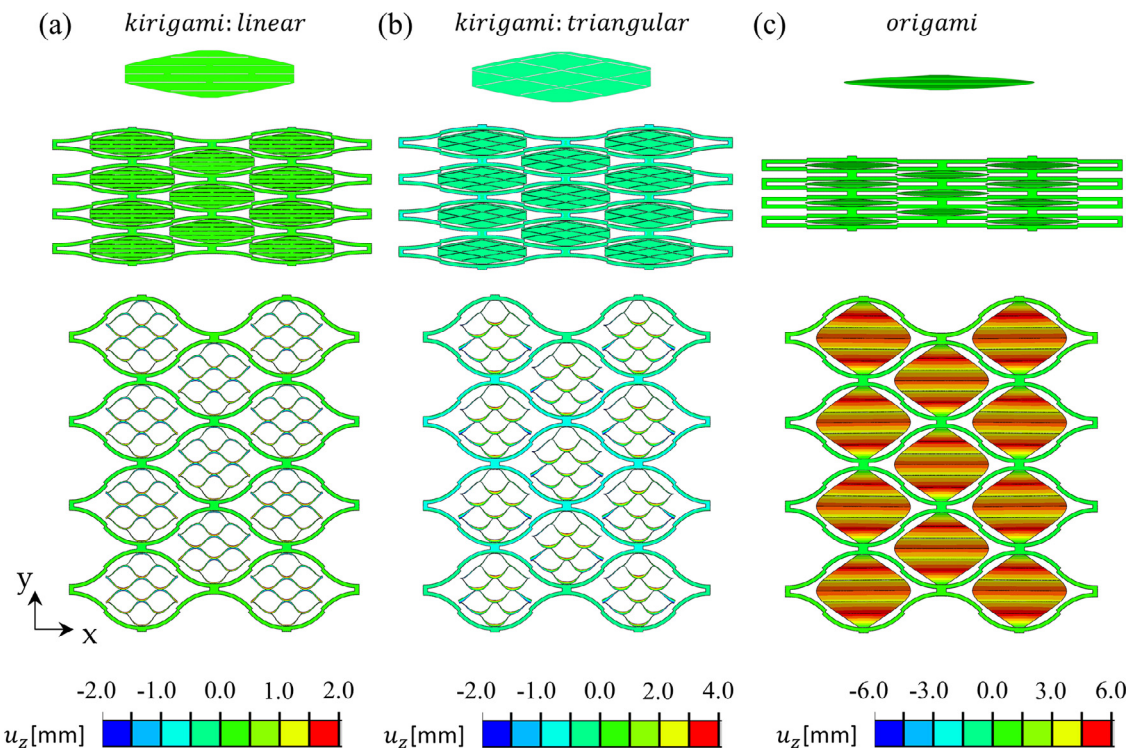

Fig. 9. Deformation snapshots of the finite-size self-deployable reflectors at the initial and deformed state, numerically reproducing the experiments reported in [34]. The distribution of the normalized out-of-plane displacement u_z is also given in the deformed configuration.

the meshings of the frame and the kirigami films should be generated simultaneously before the running of the whole simulation. Fortunately, this problem can be circumvented by making use of the features available in the software through the following two-step scheme. (*i*) Both the frame and the kirigami films are assembled and meshed. The interaction between the two parts is deactivated and the kirigami mesh is removed with the function, "model change, remove". Upon heating, only the SMA actuated frame deforms and retains a small predeformation strain, say $\varepsilon = 0.01$, while the kirigami film remains inert and in a stress-free state; (*ii*) The interaction between the two parts is activated and the kirigami film mesh is added with the function, "model change, add". From this point, the two parts are tied together and further opening of the soft deployable structure therefore actuate the deformation of the kirigami film. Differently, the origami reflector can be simulated straightforwardly because the origami film is folded to match the initial shape of the soft deployable structure where $\varepsilon = 0$.

The cuts in the kirigami films are modeled as thin rectangular slits with a thickness of 0.2 mm and an imperfection is introduced. This is done by applying two opposing small bias forces normal to the kirigami film plane at the longer side of each cut during the initial increment of this step to trigger the out-of-plane buckling deformation [4]. For the simulation of origami reflectors, the above two-step scheme is unnecessary and the simulation can be performed readily as long as the creases in origami films are properly treated. The creases were modeled using pin constraints to connect every pair of neighboring nodes on neighboring plates. A torsional spring constraint was applied to each pair of nodes, using spring-dashpot objects. The spring stiffness assigned to each pair of nodes, k, was set to be 0.001 N/rad in this study [51,52]. In all of our simulations, the kirigami/origami films are discretized using 4-node rectangular shell elements with reduced integration (Abaqus element type S4R).

Fig. 8 shows the cut shape and folding pattern of the kirigami/origami films together with the deployment process of a reflector unit and Fig. 9 shows the deformation snapshots of finite-size self-deployable reflectors in the initial and deformed state with distribution of out-of-plane displacement, quantitatively imitating the experiments reported in [34]. Two different kirigami patterns (i.e., linear pattern and triangular pattern) and one origami folding pattern are proposed to demonstrate the robustness of the numerical strategy. It should be pointed out that only kirigami/origami reflectors with linear pattern were proposed and experimentally demonstrated in [34]. Our contribution not only provides insights into the working principles and the deployment process of these kirigami/origami reflectors, but also gives new designs, such as the kirigami reflectors with triangular pattern designs in the columns of Fig. 8(b) and Fig. 9(b). This clearly shows that simulation could aid design and optimize this system and may also exploit new possibilities.

5. Concluding remarks

Marrying the ideas of smart soft composite-enabled deployable structures and kirigami/origami principles leads to self-deployable reflectors that can fold and deploy on demand. To date, the development of such self-deployable systems remains largely an empirical process. To enable the research community to deterministically design and optimize new soft deployable structures and provide information on their performance prior to manufacturing, in this study, an analytical model as well as a FEM based numerical model are developed for modeling a specific class of soft deployable structures, i.e., the SMA-based soft deployable structures. The FEM models provide the ability to analyze the performance of these SMA-enabled deployable structures and highlight the effect of geometric design parameters on the deployment process. Alternatively, the simplified analytical model offers a means of predicting the deployment process with explicit/implicit relationships between the recovery strain of SMA wires, bending curvature of individual segments, and macroscopic strains of deployable structures. More specifically, our results indicate that:

(*i*) The bending curvature of each individual segment is strongly affected by the segment thickness but is only marginally affected by the segment length, and for a given value of applied SMA recovery strain ε,

a decrease in segment thickness t results in a larger bending curvature κ for individual segments; while (*ii*) the macroscopic strains of each deployable unit cell are affected by both the segment thickness and the segment length. For a given value of applied SMA recovery strain ε, a decrease in segment thickness t or an increase in segment length L leads to a larger absolute value of $\bar{\varepsilon}_{xx}$ and $\bar{\varepsilon}_{yy}$, which indicates a wider opening of the deployable unit cell.

We also note that the design concept of integrating soft deployable frames with kirigami/origami films is realized numerically through three types of self-deployable kirigami/origami reflectors. Both reflector units as well as finite-size reflector structures are demonstrated successfully. We expect our work to open the door for further simulation-based studies of self-deployable systems with multimodal functionalities. In particular, the proposed numerical strategy may serve as a platform to accelerate the design of devices such as mechanical metamaterials [4,6,53], soft deployable structures-based robots [35], soft honeycomb actuators [54], and space solar power initiative [55–57].

Declaration of Competing Interest

The authors declare that they do not have any financial or nonfinancial conflict of interests.

CRediT authorship contribution statement

Ning An: Methodology, Formal analysis, Investigation, Writing - original draft. **Meie Li:** Conceptualization, Writing - review & editing. **Jinxiong Zhou:** Conceptualization, Writing - review & editing.

Acknowledgement

This research is supported by Natural Science Foundation of China (grant 11972277), and by a technological project of Institute of Systems Engineering, China Academy of Engineering Physics (2017KJZ06).

References

[1] Schenk M, Guest SD. Geometry of miura-folded metamaterials. Proc Natl Acad Sci USA 2013;110(9):3276–81.
[2] Choi GP, Dudte LH, Mahadevan L. Programming shape using kirigami tessellations. Nat Mater 2019;18(9):999–1004.
[3] Wang F, Guo X, Xu J, Zhang Y, Chen C. Patterning curved three-dimensional structures with programmable kirigami designs. J Appl Mech 2017;84(6):61007.
[4] An N, Domel AG, Zhou J, Rafsanjani A, Bertoldi K. Programmable hierarchical kirigami. Adv Funct Mater 2019;30(6):1906711.
[5] Rafsanjani A, Pasini D. Bistable auxetic mechanical metamaterials inspired by ancient geometric motifs. Extreme Mech Lett 2016;9:291–6.
[6] Rafsanjani A, Zhang Y, Liu B, Rubinstein SM, Bertoldi K. Kirigami skins make a simple soft actuator crawl. Sci Robot 2018;3(15):eaar7555.
[7] Rafsanjani A, Bertoldi K, Studart AR. Programming soft robots with flexible mechanical metamaterials. Sci Robot 2019;4(29):eaav7874.
[8] Wilson L, Pellegrino S, Danner R. Origami sunshield concepts for space telescopes. In: Proceedings of the 54th AIAA/ASME/ASCE/AHS/ASC Structures, Structural Dynamics, and Materials Conference; 2013. p. 1594.
[9] Ferraro S, Pellegrino S. Self-deployable joints for ultra-light space structures. In: Proceedings of the 2018 AIAA Spacecraft Structures Conference. Kissimmee, USA: AIAA; 2018. p. 694.
[10] Tachi T. Origamizing polyhedral surfaces. IEEE T Vis Comput Gr 2009;16(2):298–311.
[11] Tachi T. Designing freeform origami tessellations by generalizing resch's patterns. J Mech Des 2013;135(11):111006.
[12] Peraza Hernandez E, Hartl D, Lagoudas D. Design and simulation of origami structures with smooth folds. P Roy Soc A-Math Phy 2017;473(2200):20160716.
[13] Hernandez EAP, Hartl DJ, Lagoudas DC. Tuck-folding method for the design of origami structures with smooth folds. In: Active Origami. Springer; 2019. p. 293–330.
[14] Xu Z, Fan Z, Fu H, Liu Y, Zi Y, Huang Y, et al. Optimization-based approach for the inverse design of ribbon-shaped three-dimensional structures assembled through compressive buckling. Phys Rev Appl 2019;11(5):54053.
[15] Liu X, Georgakopoulos SV, Rao S. A design of an origami reconfigurable QHA with a foldable reflector [antenna applications corner]. IEEE Antenn Propag M 2017;59(4):78–105.
[16] Salazar R, Murthy S, Pellazar C, Stoica A. Transformers for lunar extreme environments: Large origami deployable solar reflectors. In: Proceedings of the 2017 IEEE Aerospace Conference. Big Sky, USA: IEEE; 2017. p. 1–7.
[17] Schenk M, Viquerat AD, Seffen KA, Guest SD. Review of inflatable booms for deployable space structures: packing and rigidization. J Spacecraft Rockets 2014;51(3):762–78.
[18] Silverberg JL, Na J-H, Evans AA, Liu B, Hull TC, Santangelo CD, et al. Origami structures with a critical transition to bistability arising from hidden degrees of freedom. Nat Mater 2015;14(4):389.
[19] Zheng WJ, An N, Yang JH, Zhou J, Chen YM. Tough al-alginate/poly (n-isopropylacrylamide) hydrogel with tunable lcst for soft robotics. ACS Appl Mater Interfaces 2015;7(3):1758–64.
[20] Kotikian A, McMahan C, Davidson EC, Muhammad JM, Weeks RD, Daraio C, et al. Untethered soft robotic matter with passive control of shape morphing and propulsion. Sci Robot 2019;4(33):Art-No.
[21] Yuan C, Roach DJ, Dunn CK, Mu Q, Kuang X, Yakacki CM, et al. 3D printed reversible shape changing soft actuators assisted by liquid crystal elastomers. Soft Matter 2017;13(33):5558–68.
[22] Ambulo CP, Burroughs JJ, Boothby JM, Kim H, Shankar MR, Ware TH. Four-dimensional printing of liquid crystal elastomers. ACS Appl Mater Interfaces 2017;9(42):37332–9.
[23] Kim H-S, Lee J-Y, Chu W-S, Ahn S-H. Design and fabrication of soft morphing ray propulsor: undulator and oscillator. Soft Robot 2017;4(1):49–60.
[24] Neville RM, Chen J, Guo X, Zhang F, Wang W, Dobah Y, et al. A kirigami shape memory polymer honeycomb concept for deployment. Smart Mater Struct 2017;26(5):05LT03.
[25] Jin H, Dong E, Alici G, Mao S, Min X, Liu C, et al. A starfish robot based on soft and smart modular structure (SMS) actuated by SMA wires. Bioinspir Biomim 2016;11(5):56012.
[26] Kim H-I, Han M-W, Song S-H, Ahn S-H. Soft morphing hand driven by sma tendon wire. Compos Part B-Eng 2016;105:138–48.
[27] Bellouard Y. Shape memory alloys for microsystems: A review from a material research perspective. Mat Sci Eng A-Struct 2008;481:582–9.
[28] Hartl D, Lagoudas D. Thermomechanical characterization of shape memory alloy materials. In: Shape memory alloys. Boston, USA: Springer; 2008. p. 53–119.
[29] Ahn S-H, Lee K-T, Kim H-J, Wu R, Kim J-S, Song S-H. Smart soft composite: An integrated 3d soft morphing structure using bend-twist coupling of anisotropic materials. Int J Pr Eng Man-Gt 2012;13(4):631–4.
[30] Rodrigue H, Wang W, Bhandari B, Han M-W, Ahn S-H. Cross-shaped twisting structure using SMA-based smart soft composite. Int J Pr Eng Man-Gt 2014;1(2):153–6.
[31] Rodrigue H, Wang W, Bhandari B, Han M-W, Ahn S-H. SMA-based smart soft composite structure capable of multiple modes of actuation. Compos Part B-Eng 2015;82:152–8.
[32] Rodrigue H, Wang W, Kim D-R, Ahn S-H. Curved shape memory alloy-based soft actuators and application to soft gripper. Compos Struct 2017;176:398–406.
[33] Wang W, Rodrigue H, Ahn S-H. Deployable soft composite structures. Sci Rep 2016;6:20869.
[34] Wang W, Li C, Rodrigue H, Yuan F, Han M-W, Cho M, et al. Kirigami/origami-based soft deployable reflector for optical beam steering. Adv Funct Mater 2017;27(7):1604214.
[35] Wang W, Kim N-G, Rodrigue H, Ahn S-H. Modular assembly of soft deployable structures and robots. Mater Horiz 2017;4(3):367–76.
[36] Shah SIH, Lim S. Thermally beam-direction-and beamwidth-switchable monopole antenna using origami reflectors with smart shape memory polymer hinges. IEEE Antenn Wirel Pr 2019;18(8):1696–700.
[37] Peraza-Hernandez EA, Hartl DJ, Malak Jr RJ, Lagoudas DC. Origami-inspired active structures: a synthesis and review. Smart Mater Struct 2014;23(9):94001.
[38] Kuribayashi K, Tsuchiya K, You Z, Tomus D, Umemoto M, Ito T, et al. Self-deployable origami stent grafts as a biomedical application of ni-rich tini shape memory alloy foil. Mat Sci Eng A-Struct 2006;419(1–2):131–7.
[39] Rodrigue H, Wang W, Han M-W, Kim TJ, Ahn S-H. An overview of shape memory alloy-coupled actuators and robots. Soft Robot 2017;4(1):3–15.
[40] Cisse C, Zaki W, Zineb TB. A review of constitutive models and modeling techniques for shape memory alloys. Int J Plast 2016;76:244–84.
[41] Boyd JG, Lagoudas DC. A thermodynamical constitutive model for shape memory materials. part i. the monolithic shape memory alloy. Int J Plast 1996;12(6):805–42.
[42] Lagoudas DC, Bo Z, Qidwai MA. A unified thermodynamic constitutive model for sma and finite element analysis of active metal matrix composites. Mech Compos Mater Struct 1996;3(2):153–79.
[43] Peraza-Hernandez E, Hartl D, Malak R. Simulation-based design of a self-folding smart material system. In: Proceedings of the ASME 2013 International Design Engineering Technical Conferences and Computers and Information in Engineering Conference. American Society of Mechanical Engineers Digital Collection; 2013.
[44] Hartl DJ, Lagoudas DC. Aerospace applications of shape memory alloys. Proceedings of the Institution of Mechanical Engineers, Part G: J Aerospace Eng 2007;221(4):535–52.
[45] Song S-H, Lee H, Lee J-G, Lee J-Y, Cho M, Ahn S-H. Design and analysis of a smart soft composite structure for various modes of actuation. Compos Part B-Eng 2016;95:155–65.
[46] Jung B-S, Kong J-P, Li N, Kim Y-M, Kim M-S, Ahn S-H, et al. Numerical simulation and verification of a curved morphing composite structure with embedded shape memory alloy wire actuators. J Intel Mat Syst Str 2013;24(1):89–98.
[47] Akbari S, Sakhaei AH, Panjwani S, Kowsari K, Serjourei A, Ge Q. Multimaterial 3d printed soft actuators powered by shape memory alloy wires. Sensor Actuat A-Phys 2019;290:177–89.
[48] Lagoudas D, Bo Z, Qidwai M, Entchev P. Sma um: user material subroutine for thermomechanical constitutive model of shape memory alloys. Texas A&M University College Station TX 2003.

[49] Xu L, Baxevanis T, Lagoudas DC. A three-dimensional constitutive model for the martensitic transformation in polycrystalline shape memory alloys under large deformation. Smart Mater Struct 2019;28(7):74004.
[50] Pratt V. Direct least-squares fitting of algebraic surfaces. ACM SIGGRAPH Comput Graph 1987;21(4):145–52.
[51] Boatti E, Vasios N, Bertoldi K. Origami metamaterials for tunable thermal expansion. Adv Mater 2017;29(26):1700360.
[52] Grey SW, Scarpa F, Schenk M. Strain reversal in actuated origami structures. Phys Rev Lett 2019;123(2):25501.
[53] Dias MA, McCarron MP, Rayneau-Kirkhope D, Hanakata PZ, Campbell DK, Park HS, et al. Kirigami actuators. Soft Matter 2017;13(48):9087–92.
[54] Guiducci L, Fratzl P, Bréchet YJ, Dunlop JW. Pressurized honeycombs as soft-actuators: a theoretical study. J R Soc Interface 2014;11(98):20140458.
[55] Kelzenberg MD, Espinct-Gonzalez P, Vaidya N, Roy TA, Warmann EC, Naqavi A, et al. Design and prototyping efforts for the space solar power initiative. In: Proceedings of the 2017 IEEE 44th Photovoltaic Specialist Conference (PVSC). Washington, DC: IEEE; 2017. p. 558–61.
[56] Vaidya N, Kelzenberg MD, Espinet-González P, Vinogradova TG, Huang J-S, Leclerc C, et al. Lightweight carbon fiber mirrors for solar concentrator applications. In: Proceedings of the 2017 IEEE 44th Photovoltaic Specialist Conference (PVSC). Washington, DC: IEEE; 2017. p. 572–7.
[57] Arya M, Lee N, Pellegrino S. Ultralight structures for space solar power satellites. In: Proceedings of the 3rd AIAA Spacecraft Structures Conference. San Diego, USA: AIAA; 2016. p. 1950.